The advantage of reflectance measurements in radiometric adjustment of aerial imagery

Susanne Scholz (Vexcel Imaging GmbH, Anzengrubergasse 8, 8010 Graz, susanne.scholz@vexcel-imaging.com)
Marc Muick (Vexcel Imaging GmbH, Anzengrubergasse 8, 8010 Graz, marc.muick@vexcel-imaging.com)

Keywords: absolute radiometry, reflectance, UltraCam, aerial imagery, radiometric adjustment, ground truth measurements.

Abstract

The radiometric adjustment of aerial imagery is a process of very high importance considering the influences this step can generate not only on the look of the image data (white balance), but even more importantly on derived information like indices (NDVI). In comparison to the Aerial Triangulation where it is relatively straight forward to set up thresholds that need to be met in order to achieve a high-quality result, the world of radiometric adjustment is dramatically different. There is no single standard or guideline that dictates what a high-quality radiometric result will look like. Apart from these challenges there is also a rather big gap between the rich and longstanding academic work done in the field of radiometry and actual application in real-life projects. The biggest discrepancy is the usage of single images, especially when dealing with absolute radiometry approaches versus multiple thousand color balanced images in a single block in an actual production environment. In this paper, we present the advantages of utilizing reflectance measurements as a method to stabilize radiometric adjustments, as well as utilizing them as anchor to create indices like the NDVI that correspond to the value range given by literature.

1. Introduction

In the field of radiometry, when terms like radians, absolute radiometry, and reflectance are concerned, those methods usually result in multiplicative correction factors and offsets applied per spectral channel. It can be argued that a human radiometric operator could derive a solution that closely approximates the outcome of the methodology presented in this paper. Such an approach would also result in derived products, such as NDVI, falling within value ranges commonly reported in the literature. Although it is possible to achieve such results without the use of a reflectance target, questions remain regarding the consistency with which this can be accomplished in an operational aerial data production environment. The likelihood of success is strongly dependent on the experience level of the radiometric operator and on the specifications defined by the end user. These specifications may, for example, emphasize a particular visual appearance of the imagery, thereby neglecting the requirements for accurate indices computation. Furthermore, in large-scale aerial projects, such as national tenders, multiple data providers are often involved. In such cases, the probability of achieving highly comparable radiometric processing across providers is low, and guided or standardized methods are therefore expected to yield superior consistency.

In this paper we will propose a method for radiometric adjustment of aerial images, which includes the advantage that the resulting images are in reflectance unit. This makes the images comparable to other remote sensing products as well as vegetation indices as for example the NDVI can be computed and compared to other sensor indices.

A typical absolute radiometric workflow with a testflight data set will be presented. To assure a correct absolute radiometric workflow ground truth reflectance measurements were taken with a spectrometer during the flight mission (Hakala, 2018). Further aerial image data sets with no reference measurements on the ground were available. Information about the sun azimuth and altitude angle was available as well. A model to compute estimated reflectance values based on sun azimuth and measured grey surface reflectances was build. This model was used to derive reflectance scale factors per spectral channel, for the flight missions that did not feature a ground truth measurement with a spectrometer. The results are compared to the reference project as well as to satellite images.

The structure of this paper is as follows: first the data, measurements and processing of all collected data is described in detail in section 2. Section 3 describes the reflectance estimation model itself, the methodology to compute reflectance images and the derivation of the corresponding reflectance values – which are the basis for the analysis in section 4. Section 5 gives a summary of the results and an outlook on the ideas for further improvement.

2. Data description & processing information

Every UltraCam camera system that is delivered to a customer is test flown over a test field area. This gives Vexcel Imaging GmbH the unique possibility to evaluate images from all kinds of different lightning situations and times of the year. The image catalogue collected here features a tremendous amount of imagery. Images with different ground sampling distances (GSDs) and sensors, Bayerpattern as well as monochrome sensors over UltraCam generations at various lightning situations and seasons.

2.1. Ground truth

Over the past years multiple radiometric ground truth measurements including color and reflectance targets during several UltraCam test flights were collected, utilizing a calibrated Avantes spectrometer (AVASPEC-ULS2048-USB2-FC/PC). The reflectance targets are on the one hand a Spectralon white (99% reflectance) target and a 50% reflectance grey target (RTI of SphereOptics). Further measurements with the spectrometer of different asphalts and other surfaces (gravel, paving, vegetation, bare soil, etc.) at different sun angles have been performed. Figure 1 shows the color and reflectance target setup in the testflight area of Gleisdorf. The collected measurements are used as a basis for the computed model of reflectances depending on sun azimuths and further investigations and analysis in this paper.

Figure 1. Color and reflectance target measurements during an aerial flight mission

2.2. Image Data

The image data used in this analysis comes from 4 different flights. The reference flight took place on October 22nd, 2024. There an UltraCam Osprey 4.1. (UCO 4.1) was flown over the area of Gleisdorf, Austria. The Ground Sampling Distance (GSD) was 5cm. The flight took place at sunny weather at around noon. During the testflight color and reflectance targets were placed and spectrometer measurements were performed, including the targets and surrounding features parallel to the flight.
Three further datasets were chosen to verify the suggested method. The projects are located in different parts of the earth and have different sun angles to our reference dataset. Two datasets have also been flown with an UCO 4.1, and one dataset was collected from an UCC 4.1 (UltraCam Condor 4.1.). The areas are Gijon, Spain and Murfreesboro, Tennessee (US) and Sandy Springs, Georgia in the US. An overview of the chosen images and the corresponding details of the datasets can be found in Table 1.
For all images comparable Sentinel reflectance images are available, which were recorded on the same day or a day near the aerial image collection (Yu,2016).

Area	Gleisdorf	Gijon		Murfreesboro	Sandy Springs	
	AUT	ESP		TN, USA	GA, USA	
Sensor	UCOv41	UCOv41		UCCv41	UCOv41	
ImgNo	319	12194	3935	313	15674	25061
Date	22.10.2024	08.11.2024	16.09.2024	13.04.2024	01.12.2024	25.12.2024
Time	10:43:09	10:56:33	15:26:40	19:39:56	16:09:13	16:33:13
Sun Altitude	31.62°	27.59°	39.86°	60.96°	31.17°	30.69°
Sentinel Img	21.10.2024	06.11.2024		13.04.2024	24.11.2024	
Time	10:00:41	11:11:49		16:19:29	16:26:21	

Table 1. Overview Testdata

The images are not absolutely corrected (no absolute calibration coefficient is being applied) but still radiometrically (dark current, pixel gain, vignetting) and geometrically corrected. In addition, they have been processed with UltraMap software suite up to a stage (Level 03) where the panchromatic images are fused with the multispectral data (pan-sharpened) and the value of the single pixels remain DN.
The post processed and pan-sharpened images are exported with no further radiometric changes – meaning there was no user interaction with setting of highlight and shadow values, level settings or curves when exporting the resulting images. The output images have the full unchanged radiometric resolution in 16bit.

2.3. Reference Data

The reference data set (UCO 4.1 – Gleisdorf) is being processed with UltraMap to get radiometrically (dark current, pixel gain, vignetting) and geometrically correct images but the multispectral images are not pansharpened and fused with the panchromatic image (Ladstädter, 2010). At this stage (Level 02 images) the imagery is still separated between the high-resolution panchromatic information and multispectral information. Again, the output images have the full unchanged radiometric resolution in 16bit without any other incorporated information as the panchromatic channel – pure radiometrically corrected signal of the system. Again no user interaction was performed –no curves, no level editing etc. have been applied to the images (Remondino, 2025).
Absolute calibration coefficients (Ryan and Pagnutti, 2009) were derived in calibration and used to convert image DNs to radiance, to have the image data in the physical unit of W/m^2 sr µm. In a further step the ground measurements of the reflectance target and surrounding grey surfaces (different kinds of asphalt) are used to compute the reflectance images (see next section). This workflow represents a correct absolute radiometric workflow (Schläpfer, 2023).

3. Methodology

The generic term for pixel values is **Digital Number** or **DN**. It is commonly used to describe pixel values that have not yet been calibrated into physically meaningful units (Zaman, 2014). **Radiance** is the amount of radiation coming from an area. It is measured in watts per steradian per square metre (W/sr m ^{2}). To derive a radiance image from an uncalibrated image, typically a gain and offset (calibration coefficients) must be applied to the pixel values (Beisl, 2006 and Schläpfer, 2020). Radiance includes radiation reflected from the surface, bounced in from neighbouring pixels, and reflected from clouds above the area of the pixel. Radiance is also affected by the source of radiation, which is for optical imagery the sun. **Reflectance** (Beisl, 2008) is the proportion of the radiation striking a surface to the radiation reflected of it. Some materials can be identified by their reflectance spectra, so it is common to correct an image to reflectance as a first step towards locating or identifying features in an image. In other words, reflectance is a property of the material and its surface structure being observed. Radiance, on the other hand, depends on the illumination (both its intensity and direction), the orientation and position of the target and the path of the light through the atmosphere (Schaepman-Strub G, 2009).

Two different methods to derive reflectance images out of aerial images are used in this paper.
1) Scale factor (SF)
2) Empirical line method (ELM)
Both are well researched, fast and reliable methods to compute reflectance images out of aerial images (Richter, 2023). In a correct absolute radiometric workflow radiance images are computed, and ground truth measurements are used. The radiances in the images are set into comparison with field reflectance measurements of known reflectances (e.g. reflectance targets).
For the Empirical Line Method (Pompilio, 2017) two or three targets of different grey scales are necessary, in the best case these are a 99%-target (white), a 50%-grey target and a 10%-target (black) (ReSe Applications, 2025). With at least two calibration targets a linear equation per channel can be computed with gain and offset to convert image radiance to reflectance values as shown in Equation 1 below.

$L_{b1,2} = a_b + b_b\, \rho_{b1,2}$ *where*

$$a_b = L_{b1} - b_b \ \rho_{b1}$$
$$b_b = (L_{b2} - L_{b1}) / (\rho_{b2} - \rho_{b1}), \quad (1)$$

where L_b is the at-sensor radiance per band (1), (2) for bright, dark target
a_b is the intercept per band
b_b is the slope per band
ρ_b is the surface reflectance per band

The scale factor method (Thompson, 2016 and Wang, 2015) is the less accurate one but as long as the imaging system is linear – which the UltraCam systems are - good results can be achieved. The formula for scale factor computation can be found in Equation 2.

$$SF_b = \rho_b / DN_b, \quad (2)$$

where SF_b is the scale factor per band
ρ_b is the surface reflectance per band
DN_b is the DN per band

The main advantage of this method is that asphalt reflectances can be estimated when there are no ground truth measurements available. Those estimations are used as reference to compute the scale factors (Honkavaara, 2014) for the conversion of reflectance images This is a straightforward workflow as asphalt can be found in nearly every aerial image scene. Still the user needs to be aware of selecting the correct area of asphalt (Honkavaara, 2010). Sometimes asphalts have coloured inclusions of different stones. These samples shall be avoided as they produce incorrect reflectance values. A good advice is to check on streetside data as Google Maps to verify the asphalt chosen if the ground truth is not known.

3.1. Reflectance measurements & model for reflectance estimation

Spectrometer measurements of reflectance targets and other grey surfaces like different kinds of asphalts have been performed over the past few years at different sun altitude/azimuth angles. In Figure **2** a selection of the reflectance measurements with the spectrometer of the 50% grey target are shown. The sun azimuths vary from 20° up to 65° - which shall represent the complete range of sun angles which are typically used during image flights. The colors of the columns indicate the time of the year when the measurements were performed. Light green represents spring, dark green summer, brown is for autumn and blue represents the winter season. The upper chart shows the variation of the sun azimuth, whereas the lower chart shows the changing of the reflectance measurements of the 50%-grey target.

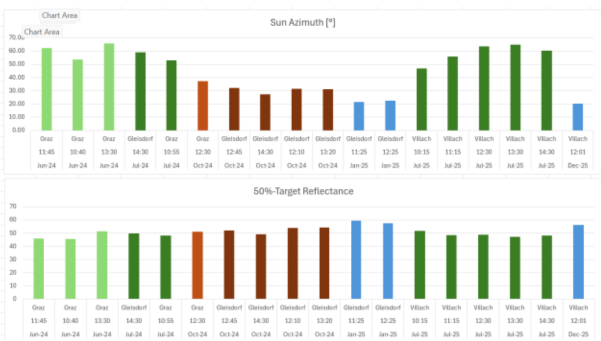

Figure 2. Overview of a selection of reflectance measurements over the year

These variations in reflectances of the diffuse target are expected and due to the variation in the illumination (especially at low solar elevations), the viewing geometry and the good but even not perfect Lambertian surface of the 50%-grey target (Honkavaara, 2012 and Kedzierski, 2019).

For this reasons all those measurements were used to create a model for reflectance values estimation. Besides the sun azimuth reflectance measurements, information about the spectral sensitivity of the UltraCam camera models have been incorporated in the model. Figure 3 shows a graph of reflectance measurements vs. sun azimuth for UCO 4.1 cameras for all four available bands (red, green, blue and near infrared).

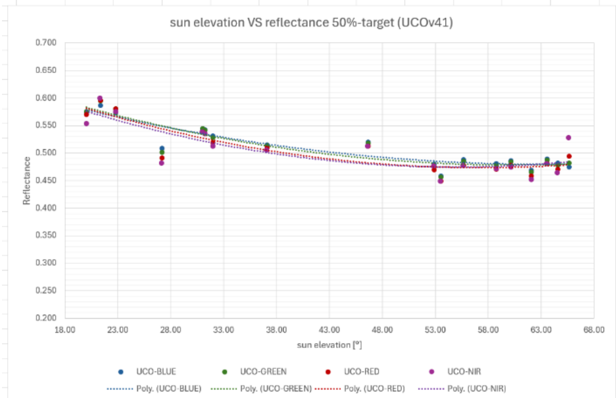

Figure 3. Reflectance measurements vs. sun azimuth for UCO 4.1

To be able to incorporate the aerial camera sensitivity to achieve more accurate reflectance measurements the measured reflectance values have been integrated over the cameras (in this case UCO 4.1 and UCC 4.1) spectral sensitivity curve (SSC – see Figure 4). This is being performed for each color channel separately (Inband reflectance values) as it can be seen in Equation 3.

$$InBandRef_b = \frac{\int_{380\,nm}^{1000\,nm} (ref_{std} * SSC_{bnorm}) d\lambda}{\int_{380\,nm}^{1000\,nm} (SSC_{bnorm})\, d\lambda}, \quad (3)$$

where $InBandRef_b$ is the InBand Reflectance per band
ref_{std} measured reflectance of the target
SSC_{bnorm} norm. SSC of the camera per band

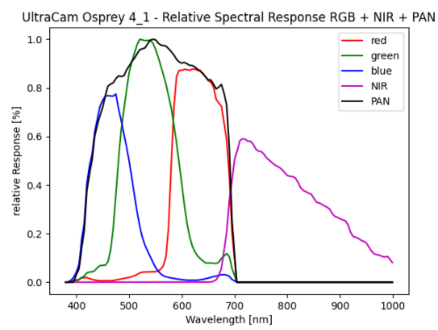

Figure 4. Relative spectral sensitivity curve of an UltraCam Osprey 4.1

The resulting reflectances per dataset for each color channel is listed in Table 2. The Gleisdorf reflectances (grey line) have not been estimated but measured during the flight mission. The second line is the reflectance estimates based on the model for Gleisdorf.

	Reflectance[%]				
	Area	RED	GREEN	BLUE	NIR
dark asphalt	Gleisdorf*	7.912	6.957	5.931	8.094
	Gleisdorf	8.013	6.897	6.013	8.265
	Gijon	7.769	6.653	5.712	7.937
	Gijon	8.511	7.396	6.627	8.935
	Murfreesboro	9.788	8.672	8.201	10.653
	Sandy Springs	7.985	6.870	5.979	8.228
	Sandy Springs	7.956	6.841	5.943	8.189
bright asphalt	Gleisdorf*	12.864	11.478	9.802	13.464
	Gleisdorf	13.251	11.876	10.151	13.943
	Gijon	12.559	11.132	9.325	13.161
	Gijon	14.667	13.399	11.839	15.543
	Murfreesboro	18.292	17.298	16.163	19.638
	Sandy Springs	13.174	11.793	10.059	13.856
	Sandy Springs	13.092	11.704	9.960	13.763

Table 2. Computed reflectances for available data sets (grey line is not estimated but measured reflectance in Gleisdorf)

When comparing the measured with the estimated reflectance values out of the model it gives very promising results. Table 3 shows the results. In this case the measured reflectance values have not been incorporated into the computation of the model. The differences between estimated and measured reflectances are all below 0.5%.

	Reflectance[%]				
	Area	RED	GREEN	BLUE	NIR
dark asphalt	Gleisdorf*	7.912	6.957	5.931	8.094
	Gleisdorf	8.013	6.897	6.013	8.265
	difference	**-0.100**	**0.060**	**-0.082**	**-0.171**
bright asphalt	Gleisdorf*	12.864	11.478	9.802	13.464
	Gleisdorf	13.251	11.876	10.151	13.943
	difference	**-0.387**	**-0.398**	**-0.349**	**-0.480**

Table 3. Measured vs. estimated reflectance values in Gleisdorf

According to literature typical reflectance values (Kokaly, 2017) are for dense vegetation for example between 5 and 15% in the visual range and in the near infrared between 40 and 60%. Asphalt has typical values of 3 to 10%, whereas bare soil has values between 10 and 40%. Concrete can range from 20 to 45%.

The main advantage of reflectance images is that spectral indices (eg NDVI – Normalized Difference Vegetation Index) known from remote sensing can be computed and the results are correct and comparable to other sensors – even to satellite sensors with different spectral response curves. With the help of these indices, it is possible to estimate which areas in an image contain healthy plants, where snow or water areas are located and even different kinds of vegetation can be detected (depending on the spectral bands used in the sensors) (Sousa, 2023). In this paper the most common index of all is used – the NDVI (Xue, 2017). The formula for computing this index is as follows:

$$NDVI = (NIR - RED) / (NIR + RED), \tag{4}$$

NDVI values are ranging between -1 and 1 (Brown, 2018). Typical NDVI values are shown in Table 4.

NDVI Range	
-1.0 - 0.1	water
< 0.1	snow / ice
0.0 - 0.2	bare soil / sand / rock
0.2 - 0.5	dry grass / sparse vegetation
0.4 - 0.6	healthy grass / moderate vegetation
0.6-0.9	forest / dense vegetation
0.1-0.4	stressed vegetation

Table 4. Typical NDVI value ranges

Figure **5** shows an overview how all of the following NDVI images in this paper are classified. All samples below are classified in the same manner to be able to compare them directly.

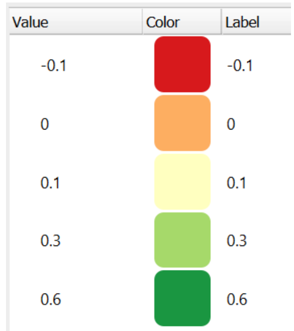

Figure 5. Legend for all following NDVI-images

4. Analysis & Results

To be able to compute scale factors for the conversion of the image DNs to reflectance it is important to select the asphalt samples with great care – that no color shifts appear in the asphalt or gravel areas. Comparisons of different grey level areas in the images is essential. In the examples shown in this paper more samples (5 to 7) per scene were chosen with focus and average values have been computed. Pixels with great discrepancy have been omitted from computation. This was performed in order to avoid exactly the selection of grey areas with potential color shifts. The measured reflectances, the known camera sensitivities (which performed the image flight – UCO 4.1 and UCC 4.1) and the known sun azimuths at the recording time of the images are the input parameters to model the reflectance values of the corresponding areas. Those reflectances are in the next step used to compute the Scale Factors for each image. And with the scale factor the corresponding reflectance images have been computed.

4.1. Reflectance computation with reference image data

The sample for a correct absolute radiometric workflow is shown in Figure **6**. It shows a scene of the Gleisdorf project. This image was treated in the correct absolute way where the images are converted to radiance, followed by the conversion to reflectance values. The upper left image (1) shows the original Level 02 image; the lower left image (3) is the computed radiance image. On the right side two reflectance images are shown – the upper right image (2) is the result of the Scale Factor conversion based on the radiance image and the lower right image (4) shows the result of the estimated Scale Factor conversion (this is already a Level03 image). All 4 images' histograms have been treated in the same way – to be able to compare them visually (no curves only shifting in the highlights).
The main problem with the correct absolute workflow is that the user is still working on the non-pansharpened image data – to be able to have the data as raw as possible to get the real sensor

response. And in addition, ground truth measurements or at least diffuse ground targets are essential.

Figure 6. Gleisdorf image, original Level02 image (1), reflectance image from Level02 image (1), radiance image (3), reflectance image (Level03) from estimated Scale Factor computation (4)

4.2. Reflectance computation based on the developed model

The absolute radiometric image workflow as described in the chapter above is time consuming and fragile and for single image processing perfect – as the results are very accurate. Although in an aerial image data production environment, where multiple thousand images need to be processed this approach is not suitable.

Aerial images that are not absolutely radiometrically corrected are in the physical unit of DN. Depending on aperture, exposure time and illumination at time of recording and the storing of image information in 8bit or 16bit, the DN range can vary. The conversion to reflectance enables a direct comparison between the images, independent from their sensor principle, as the range of the reflectances is between 0 and 100 [%]. An example is shown in Table 5. The reflectances have been converted from DNs utilizing the estimated Scale Factor values of the modelled reference reflectances. The basis for these computations was the Level03 images – with other words the pansharpened - ready for orthophoto production - images.

Sandy Springs - DN - IMG15674						
fid	Class	R	G	B	I	NDVI
1	dark asphalt	286	328	336	330	0.071
2	dark asphalt	254	286	288	344	0.151
3	bright asphalt	500	576	572	520	0.020
4	bright asphalt	414	466	454	434	0.024
5	gravel	654	716	638	682	0.021
6	gravel	220	256	264	248	0.060
7	bare soil	468	422	326	782	0.251
8	bare soil	512	486	380	836	0.240
9	dry grass	240	264	214	648	0.459
10	dry grass	316	302	248	606	0.315
11	forest	134	144	156	320	0.410
12	forest	138	142	158	354	0.439
13	urban struct	270	316	316	280	0.018
14	urban struct	466	534	518	500	0.035

Reflectance-Scale Factor - IMG15674						
fid	Class	R	G	B	I	NDVI
1	dark asphalt	6.864	6.560	5.376	7.260	0.028
6	dark asphalt	6.096	5.720	4.608	7.568	0.108
10	bright asphalt	12.000	11.520	9.152	11.440	-0.024
12	bright asphalt	9.936	9.320	7.264	9.548	-0.020
16	gravel	15.696	14.320	10.208	15.004	-0.023
21	gravel	5.280	5.120	4.224	5.456	0.016
23	bare soil	11.232	8.440	5.216	17.204	0.210
25	bare soil	12.288	9.720	6.080	18.392	0.199
29	dry grass	5.760	5.280	3.424	14.256	0.424
32	dry grass	7.584	6.040	3.968	13.332	0.275
34	forest	3.216	2.880	2.496	7.040	0.373
39	forest	3.312	2.840	2.528	7.788	0.403
41	urban struct	6.48	6.32	5.056	6.16	-0.025
43	urban struct	11.18	10.68	8.288	11	-0.008

Sandy Springs - DN - IMG25061						
fid	Class	R	G	B	I	NDVI
1	dark asphalt	670	738	724	634	-0.028
2	dark asphalt	646	702	682	808	0.111
3	bright asphalt	1224	1328	1212	1104	-0.052
4	bright asphalt	1088	1184	1062	982	-0.051
5	gravel	1922	2036	1728	1688	-0.065
6	gravel	826	884	782	810	-0.010
7	bare soil	1154	920	662	1420	0.103
8	bare soil	1330	1268	994	2146	0.235
9	dry grass	734	738	580	1606	0.373
10	dry grass	652	626	520	1082	0.248
11	forest	256	274	278	472	0.297
12	forest	316	330	330	664	0.355
13	urban struct	686	780	744	584	-0.080
14	urban struct	1352	1508	1356	1174	-0.070
					RMSE	0.088

Reflectance-Scale Factor - IMG25061						
fid	Class	R	G	B	I	NDVI
1	dark asphalt	6.700	5.904	5.068	6.974	0.020
6	dark asphalt	6.460	5.616	4.774	8.888	0.158
10	bright asphalt	12.240	10.624	8.484	12.144	-0.004
12	bright asphalt	10.880	9.472	7.434	10.802	-0.004
16	gravel	19.220	16.288	12.096	18.568	-0.017
21	gravel	8.260	7.072	5.474	8.910	0.038
23	bare soil	11.540	7.360	4.634	15.620	0.150
25	bare soil	13.300	10.144	6.958	23.606	0.279
29	dry grass	7.340	5.904	4.060	17.666	0.413
32	dry grass	6.520	5.008	3.640	11.902	0.292
34	forest	2.560	2.192	1.946	5.192	0.340
39	forest	3.160	2.640	2.310	7.304	0.396
41	urban struct	6.86	6.24	5.208	6.424	-0.033
43	urban struct	13.52	12.06	9.492	12.91	-0.023
					RMSE	0.033

Table 5. DN versus Reflectance Values in 2 overlapping images of the Sandy Springs project

Table **5** shows the DN and reflectance values of 2 overlapping images of the Sandy Springs project. As the NDVI columns in Table 5 already indicates the fitting between those 2 images is much better than when computing the NDVI in the uncorrected DN range. There are differences between the results, which is still absolutely feasible as the recording date of the images is 24 days apart from each other. The vegetation as well as the surroundings change in this period of time immensley as these images were even recorded in december on the northern hemisphere. The RMSE value computed out of the differences of the NDVIs of the overlapping areas of the two images (for the DN vs. Reflectance) shows the significant improvement. The RMSE could be reduced nearly a third. When switchitng from a quantitativ metric to a quality metric like given in a visual sense in Figure 7, it can be argued that fixing the lack of consitency in the DN results show in part 1 and 2 of Figure 7 even outweigh the already impressive quantitative RMSE improvements shown in Table 5.

The NDVI examples shown in Figure 7 are a perfect visual representation of the described relationships. This sample is from the Gijon project. The two images (left side is image 12194 shot in the beginning of November, 2024 and on the right side there is the NDVI images of image 3935 shot in the middle of September 2024) have been recorded nearly 2 months apart. The upper two images (1, 2) show the NDVI results from the uncorrected DN images and the lower two NDVI images (3, 4) show the results of the computation of the index based on the reflectance images (with estimated reflectance for Scale Factor computation). The most prominent changes can be found in urban areas and man made structures, which fit much better together than in the DN results. Also the vegetation is represented more accurate than before especially in the first example (1 to 3). The vegetation changes between the two images (3 and 4), as this is typical for this time of the year.

https://doi.org/10.5194/isprs-archives-XLIX-B3-2026-1379-2026 | © Author(s) 2026. CC BY 4.0 License.

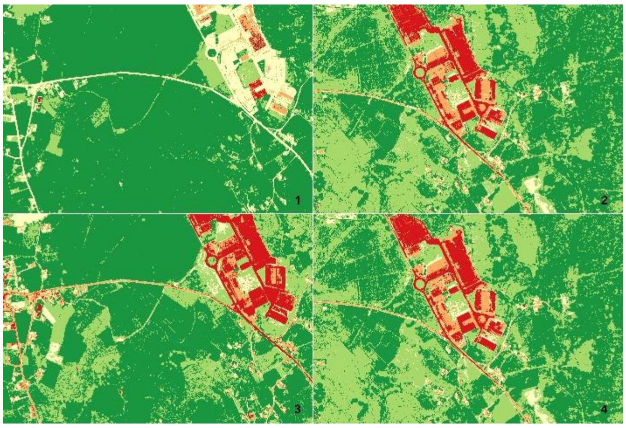

Figure 7. NDVI Results of the Gijon project (upper images are computed out of DN images, lower ones from the reflectance images)

To have a “known” reference to verify the modelled approach for the images where no ground truth measurements were available, Sentinel images of the same area recorded during the same time (as good as possible) were selected and the NDVI for those scenes were computed as well. The NDVI computed out of the reflectance images is also being compared to the one of the Sentinel images.
Figure 8 shows such an example. On both images the Sentinel NDVI image is in the background and on the upper part (1) the NDVI image of the DN image is shown in front and on the lower part (2) the reflectance NDVI result is shown.

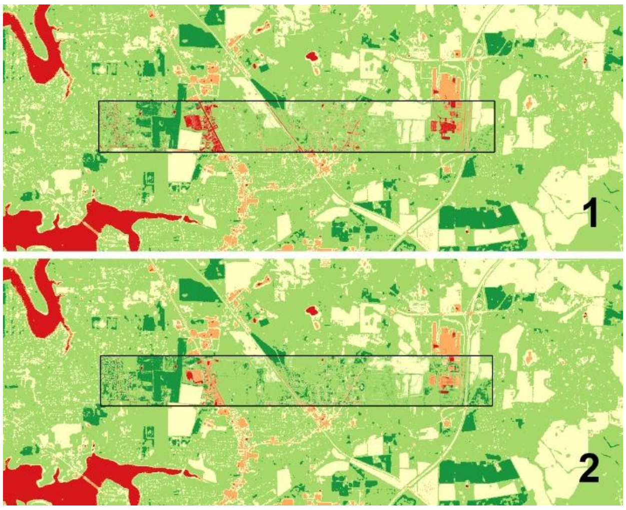

Figure 8. NDVI Images from UCC 4.1 (1 - NDVI from DN, 2 – NDVI from estimated reflectance image) compared with Sentinel NDVI for Murfreesboro project

Again, especially the urban areas fit much better to the result of the Sentinel. But also, when focusing on details in the vegetation especially when looking at the sparse vegetation the reflectance images produce more accurate results.

5. Conclusion & Future Work

This paper shows a new approach to use estimated reflectance for the Scale Factor computation to improve the radiometric quality of aerial images. With the help of the estimated scale factors images in DN space can be converted to reflectance and with this meaningful vegetation indices can be computed. Besides the vegetation indices the images are radiometrically adjusted, that minimum manual work is necessary to produce neutral looking aerial images. The study worked with different images recorded on different days in the year at different sun azimuths and on different locations on the earth. The suggested method produces more reliable results, especially with images which were recorded on different days (especially when there were several weeks in between). The biggest difference can be seen in urban areas – manmade structures as concrete surfaces, roads etc. have improved a lot (especially when compared to the Sentinel NDVI). Even though a manual selection of color shift free asphalt areas is necessary, the massive benefits of the proposed method outweigh the small room for error based on the users experience level to a very large degree.

Further tests with more sophisticated methods to compute the reflectance values as the enhanced ELM method or even reflectance computation based on a physical model of the camera showed promising first results. Detailed tests will follow to determine the best method which produces the best and most accurate results.

References

Beisl, U., 2006. Absolute spectroradiometric calibration of the ADS40 sensor. Revue Francaise de Photogrammetrie et de Teledetection. 14-18.

Beisl, U., Telaar, J., Schoenermark, M., 2008. Atmospheric correction, reflectance calibration and BRDF correction for ADS40 image data. *International Archives of the Photogrammetry, Remote Sensing and Spatial Information Sciences* 37 (B7): 169–174.

Brown, J., 2018. NDVI, the Foundation for Remote Sensing Phenology. https://www.usgs.gov/special-topics/remote-sensing-phenology/science/ndvi-foundation-remote-sensing-phenology (17 March 2026).

Hakala, T., Markelin, L., Honkavaara, E., Scott, B., Theocharous, T., Nevalainen, O., Näsi, R., Suomalainen, J., Viljanen, N., Greenwell, C., Fox, N., 2018. Direct Reflectance Measurements from Drones: Sensor Absolute Radiometric Calibration and System Tests for Forest Reflectance Characterization. *MDPI Sensors*, 18, 1417

Honkavaara, E., Hakala, T., Peltoniemi, J., Suomalainen, J., Ahokas, E., Markelin, L., 2010. Analysis of Properties of Reflectance Reference Targets for Permanent Radiometric Test Sites of High Resolution Airborne Imaging Systems. *MDPI Remote Sensing,* 2, 1892-1917.

Honkavaara, E., Markelin, L., Hakala, T., Peltoniemi, J., 2014. The Metrology of Directional, Spectral Reflectance Factor Measurements Based on Area Format Imaging by UAVs: *Photogrammetrie • Fernerkundung • Geoinformation* 3/2014, 0175–0188

Honkavaara, E., Markelin, L., Rosnell, T., Nurminen, K., 2012. Influence of solar elevation in radiometric and geometric performance of multispectral photogrammetry. *ISPRS Journal of Photogrammetry and Remote Sensing,* Vol. 67, 13-26.

Kedzierski,, M., Wierzbicki,, D., Sekrecka, A., Fryskowska,, A., Walczykowski, P., Siewert, J., 2019. Influence of Lower Atmosphere on the Radiometric Quality of Unmanned Aerial Vehicle Imagery. *Remote Sens.*, *11*, 1214. https://doi.org/10.3390/rs11101214

Kokaly, Raymond, Clark, Roger, Swayze, Gregg, Livo, K., Hoefen, Todd, Pearson, N., Wise, R., Benzel, William, Lowers, Heather, Driscoll, Rhonda. (2017). USGS Spectral Library Version 7. 10.3133/ds1035.

Ladstädter, R., Tschemmernegg, H., Gruber, M., 2010. Calibrating the Ultracam aerial camera systems - an update. Int. Arch. Photogramm. Remote Sens. Spatial Inf. Sci., XXXVIII.

Remondino F., Muick M., Cramer M., Wenzel K., Legat K. (2025). A status quo in aerial photogrammetric mapping: *The International Archives of the Photogrammetry*, Remote Sensing and Spatial Information Sciences, Volume XLVIII-1/W4-2025

Pompilio, L., Marinangeli, L., Amitrano, L., Pacci, G., D’andrea, S., Iacullo, S., Monaco, E., 2017. Application of the empirical line method (ELM) to calibrate the airborne Daedalus-CZCS scanner: *European Journal of Remote Sensing*, VOL. 51, NO. 1, 33–46

ReSe Applications LLC, 2025. DROACOR® - Drone Imagery Physical Atmospheric Correction, User Manual, Version 2.1. https://rese-apps.com/pdf/DROACOR_Manual.pdf (17 March 2026)

Richter, R, Schläpfer, D., 2023. Atmospheric and Topographic Correction. ATCOR Theoretical background, Version 1.3. https://www.rese-apps.com/pdf/atcor_atbd.pdf (17 March 2026)

Ryan, R. E., Pagnutti, M., 2009. Enhanced Absolute and Relative Radiometric Calibration for Digital Aerial Cameras. *Photogrammetric Week '09,* Wichmann Verlag, 81-90, Heidelberg, Dieter Fritsch (Ed.).

Schaepman-Strub, G., Schaepman, M.E., Martonchik, J.V., Painter, T., Dangel, S., 2009. Radiometry and Reflectance: From Terminology Concepts to Measured Quantities. The SAGE Handbook of Remote Sensing. 10.5167/uzh-26245.

Schläpfer, D., Popp, C., Richter, R., 2020. “Drone data atmospheric correction concept for multi- and hyperspectral imagery. *ISPRS - International Archives of the Photogrammetry*, Remote Sensing and Spatial Information Sciences, vol. XLIII-B3-2020, pp. 473–478, doi: 10.5194/isprs-archives-xliii-b3-2020-473-2020.

Sousa, D., Small, C., 2023. Which Vegetation Index? Benchmarking Multispectral Metrics to Hyperspectral Mixture Models in Diverse Cropland. *MDPI Remote Sensing*. 15, 971

Thompson, D.R., Roberts, D.A., Gao, B.C., Green, R.O., Guild, L., Hayashi, K., Kudela, R., Palacios, S., 2016. Atmospheric correction with the Bayesian empirical line. *OPTICS EXPRESS* 2134, Vol. 24, No. 3

Wang, C., Myint, S, Price, K., Huan, W., Nan, A., 2015. A Simplified Empirical Line Calibration Method for sUAS-based Remote Sensing.

Xue, J., Su, B., 2017: Significant Remote Sensing Vegetation Indices: AReview of Developments and Applications. *Journal of Sensors,* Volume 2017, Article ID 1353691

Yu, L., Zhang, Y., Sun, M., Zhu, X., 2016. Colour balancing of satellite imagery based on a colour reference library. *International Journal of Remote Sensing*, 37(24), 23.

Zaman, B., Jensen, A., Clemens, S.R., McKee, M., 2014. Retrieval of Spectral Reflectance of High Resolution Multispectral Imagery Acquired with an Autonomous Unmanned Aerial Vehicle: AggieAir™. *AggieAir Publications*. Paper 14